

# Content Bias in Deep Learning Age Approximation: A new Approach Towards more Explainability

Robert Jöchl and Andreas Uhl

University of Salzburg, Department of Artificial Intelligence and Human Interfaces,  
Salzburg, Austria

{robert.joechl, andreas.uhl}@plus.ac.at

## Abstract

In the context of temporal image forensics, it is not evident that a neural network, trained on images from different time-slots (classes), exploit solely age related features. Usually, images taken in close temporal proximity (*e.g.*, belonging to the same age class) share some common content properties. Such content bias can be exploited by a neural network. In this work, a novel approach that evaluates the influence of image content is proposed. This approach is verified using synthetic images (where content bias can be ruled out) with an age signal embedded. Based on the proposed approach, it is shown that a ‘standard’ neural network trained in the context of age classification is strongly dependent on image content. As a potential countermeasure, two different techniques are applied to mitigate the influence of the image content during training, and they are also evaluated by the proposed method.

## 1 Introduction

In temporal image forensics, the assumed situation is that a forensics analyst is provided with a set of chronologically ordered trusted images and a second not trustworthy set (from the same imager). The main objective is to approximate the age of images from the not trustworthy set relative to the trusted set. This age estimation is usually based on time-dependent traces that are hidden in a digital image. The most common and well-known traces in this context are in-field sensor defects. In-field sensor defects develop after the manufacturing process and accumulate over time (*i.e.*, once a pixel is defective, it no longer heals). Further characteristics of

in-field sensor defects have been studied in multiple publications (*e.g.*, [1, 2, 3, 4, 5, 6, 7]).

Since in-field sensor defects accumulate over time, the age of an image (relative to images from the same imager) can be approximated based on the detected defects present. Two methods that explicitly exploit the presence of in-field sensor defects were proposed in [8] and [9]. In both methods, the median filter residuals at defect position were used as features. Unlike these traditional techniques, a Convolutional Neural Network (CNN) learns the classification features used. Ahmed et al. utilized two well-known CNN architectures for age classification (*i.e.*, the AlexNet [10] and GoogLeNet [11]) in [12]. The authors reported an accuracy of over 85% for a five-class classification problem. In [13], we systematically investigated the influence of the presence of strong in-field sensor defects when training a CNN for age classification. Considering the investigated ‘five-crop-fusion’ scenario (where five networks are trained on different fixed image patches each) the presence of a strong in-field sensor defect turns out to be irrelevant for improving the age classification accuracy. For this reason, we suggested that other ‘age’ traces are exploited by the network.

Following the results in [13], we analyzed the device (in)dependence of the learned ‘age’ features in [14]. However, based on the results obtained, the question of device (in)dependence could not be answered. In contrast, the reported results cast doubt on whether the inference was based solely on age related features. Deep neural networks can be considered as a ‘black box’. For example, in the context of deep learning age approximation, it is not evident that the age class prediction is based solely on detected age traces. In principle, it is likely

that images taken in close temporal proximity (*e.g.*, belonging to the same age class) share some common content properties (*e.g.*, common scene properties, weather conditions or seasonal commonalities). Such non-age-related features can be exploited by the CNN to discriminate between the age classes. The features learned by a standard CNN trained in the context of image age approximation were analyzed in [15]. For this purpose, we used a method from the field of explainable artificial intelligence (XAI), *i.e.*, Class Activation Maps (CAMs). Based on this analysis, we showed that most likely the image content (*e.g.*, scene properties and light conditions) is more important for classification than the inherent age signal. However, the analysis of CAMs can become cumbersome when the influence of image content needs to be evaluated for different models.

This work is an extension of [14] and [15]. We deepen the analysis of the role of image content in the context of feature-learning based age approximation algorithms (*i.e.*, deep neural networks). For this purpose, the contribution of this work are as follows:

1. We propose a novel approach in the context of XAI and deep learning age approximation that evaluates the influence of image content.
2. We evaluate the functionality of the proposed XAI method using synthetic images (where content bias can be ruled out) with an age signal embedded.
3. Based on the proposed XAI method, we evaluate the influence of image content on a ‘standard’ CNN trained in the context of age approximation. Furthermore, we apply two different techniques to mitigate the influence of image content during training and also evaluate them using the proposed XAI approach.

The remainder of this paper is organized as follows: the proposed XAI approach is described in section 2. In section 3, the models used in the context of deep learning age approximation are explained. Experimental settings and results are stated and discussed in section 4 and the key insights are summarized in the last section 5.

## 2 Explainable Artificial Intelligence (XAI)

Deep neural networks independently learn the features used and are often superior to classical methods based on handcrafted features. However, such networks usually



Figure 1: Example of an average image, age traces like in-field sensor defects are preserved.

consist of millions of parameters, which turn the models into a ‘black box’. The field of XAI focuses on understanding and interpreting the decisions of such deep neural networks. A comprehensive survey of methods in the field of XAI is given in [16]. In the context of deep learning age approximation, the main objective is to assess whether the decision made is based on comprehensible evidence (*i.e.*, some hidden age signal) or on some exploited content bias. For this purpose, we propose a novel approach in this context.

### 2.1 Average Images

Image age approximation can be considered a multi-class classification problem, where the classes are defined by the temporal resolution of the exploited age traces and the available trusted images. For this purpose, let  $\theta \in \mathbb{R}^{h \times w}$  be the sum of age traces at a certain point in time that are embedded in an image  $Y$  of height  $h$  and width  $w$ . We assume that  $\theta$  is constant (except for small variations due to different camera settings) across all images of a given age class  $k$  and differs between the other age classes.

In contrast to  $\theta$ , the image content within a given class is more or less random. For this purpose, let  $\bar{Y}^k$  be the average image of class  $k$ , *i.e.*,

$$\bar{Y}^k(i, j) = \frac{1}{|S_k|} \sum_{Y \in S_k} Y(i, j), \quad (1)$$

where  $S_k$  represents the set of images of class  $k$ .  $i$  and  $j$  denote the pixel index. Random image content is suppressed in  $\bar{Y}^k$  while the constant age signal  $\theta$  is preserved (as shown in Figure 1). Theoretically, parts of an age signal that are very unstable in their position and whose polarity is frequently changing would also be attenuated. We assume that these properties do not apply to the hidden age signal. This also holds for known age traces (*i.e.*, in-field sensor defects). Hence, if inference

is based (solely) on a hidden age signal, the classification accuracy of average images should be similar to the accuracy of the original input (as used for training).

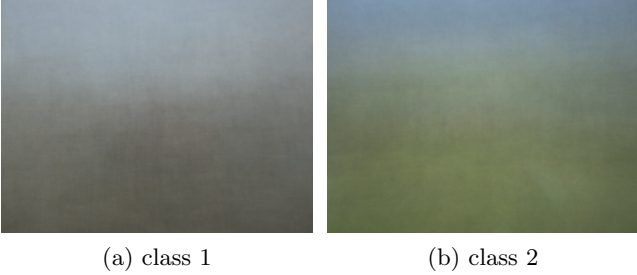


Figure 2: Example of average images.

However,  $\bar{Y}^k$  also represents the average image content. As can be seen in Figure 2 (a and b), the images of class 2 probably contain more nature scenes (green areas) whereas class 1 images probably contain more urban scenes (more gray than green). These remaining content parts can also be exploited by the model. For this reason, additionally an image representing the average color of the average image, *i.e.*,

$$\bar{Y}_c^k(i, j) = \frac{1}{h \times w} \sum_{i'=1}^h \sum_{j'=1}^w \bar{Y}^k(i', j'), \quad (2)$$

is generated. Each pixel in the image has the same value (constant component), thus, any structural components (including the age signal) are eliminated. Since the average color depends strongly on the image content, a successful discrimination of  $\bar{Y}_c^k$  would indicate that the image content is exploited by the model. The structural components only are represented by the residual image

$$\bar{Y}_r^k(i, j) = \bar{Y}^k(i, j) - \min(\bar{Y}^k). \quad (3)$$

To avoid negative values, a subtraction with the minimum value of  $\bar{Y}^k$  is performed. If  $\min(\bar{Y}^k)$  is near zero, the difference to  $\bar{Y}^k$  is marginal. A successful discrimination of  $\bar{Y}_r^k$  is expected when the model has learned to exploit an age signal. The filtered version of  $\bar{Y}^k$  is generated by,

$$\bar{Y}_f^k(i, j) = F(\bar{Y}^k(i, j)), \quad (4)$$

where  $F$  represents a median filter with kernel size 5. This filters out all high-frequency image components (*i.e.*, including in-field sensor defects), and discrimination is no longer possible based on such components. An

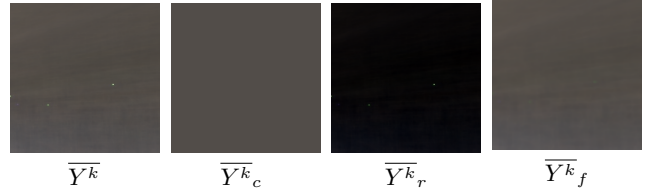


Figure 3: Example of the different variants generated.

example of all generated versions is given in Figure 3. The proposed XAI technique is a post-hoc method that aims to explain the behavior of a trained model at testing time. In other words, a model is trained on regular image data. The influence of image content on the discrimination performance is then evaluated by comparing the classification accuracy achieved when the original inputs (as used for training) and the different average images are provided.

## 2.2 Age Signal Embedded in Synthetic Images

Synthetic images are computer generated (rendered) and do not contain any artifacts or noise introduced by the image acquisition pipeline (*i.e.*,  $Y_{SYN} = I$ ). Hence, they do not exhibit an age signal. To evaluate the functionality of the proposed XAI method, the method is applied to a trained model where content bias can be ruled out. For this purpose, an age signal is embedded in synthetic images. Thus, truly identical images (in terms of image content) are available per class, with only a different version of  $\theta$  being embedded. If a model is trained on these images, the image content can be definitely ruled out and only the embedded age signal is exploited.

For this work, a subset (400 rendered images) of the Grand Theft Auto 5 dataset [17] is considered per class. A series of Dark Field Images (DFIs) acquired at different time-slots is used to estimate the age signal that is to be embedded in the rendered images. DFIs are calibration images where the shutter of the camera is closed and thus the incident light is set to zero (*i.e.*  $I = 0$ ).

In [8], Fridrich and Goljan defined the following output model of a sensor:

$$Y = I + IK + \tau D + c + \Theta, \quad (5)$$

where  $K$  denotes the Photo-response non-uniformity (PRNU),  $D$  the dark current,  $c$  a fixed offset and  $\Theta$  is a collection of all other noise sources. Since  $D$  depends on exposure time, ISO setting, and temperature, these

factors are combined into  $\tau$ . In-field sensor defects usually have a high value of  $D$  and/or  $c$ . Since the incident light is set to zero (*i.e.*  $I = 0$ ) when capturing DFIs,

$$Y_{DFI} = \tau D + c + \Theta. \quad (6)$$

Thus, only additive parameters (*e.g.*, in-field sensor defects) remain.  $\Theta$  could also contain an (unknown) age signal that is also retained. However, random parts in  $\Theta$  are mitigated through averaging a series of DFIs. Since only additive parameter remain, the estimated age signal  $\hat{\theta}_k$  of a certain class  $k$  is simply added to  $Y^{SYN}$ , *i.e.*,

$$Y_{SYN}^k = I + \hat{\theta}^k = I + \overline{\tau D}^k + \overline{c}^k + \overline{\Theta}^k. \quad (7)$$

Thus, all age traces that depend on  $I$  are not considered.

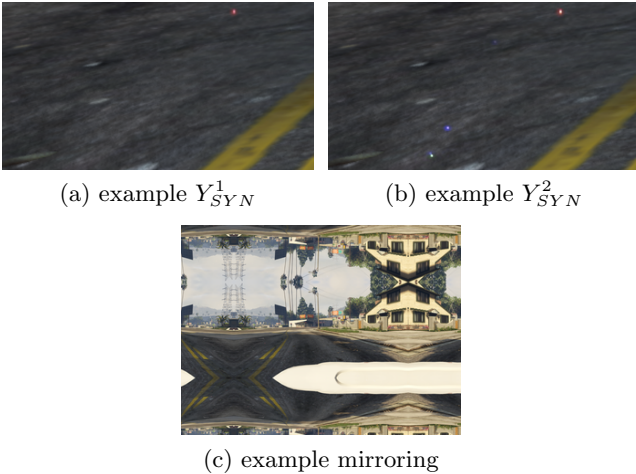


Figure 4: Example of synthetic images.

An example of the embedded age signal (in-field sensor defects) is illustrated in Figure 4 (a and b). The dimension of  $\hat{\theta}$  ( $w \times h$ ) corresponds to the pixel resolution of the camera used to capture the DFIs. However, this resolution might not correspond to the resolution of the synthetic images. To obtain a resolution corresponding to  $\hat{\theta}$ ,  $Y_{SYN}$  is expanded by mirroring the boundary regions (see Figure 4 (c)).

### 3 Deep Learning Age Approximation

In [13, 14], the idea was that the age traces can be interpreted as a signal that is hidden in a digital image. The field of image steganalysis is the science of detecting whether there is a secret message (signal) hidden

in an image. For this reason, methods proposed in the field of image steganalysis may also be suitable for detecting existing age traces. The Steganalysis Residual Network (SRNet) [18] is a model from the field of image steganalysis and has already been used in [13, 14, 15] in the context of image age approximation. The SRNet is based on the residual learning principle [19] and depicted in Fig. 5.

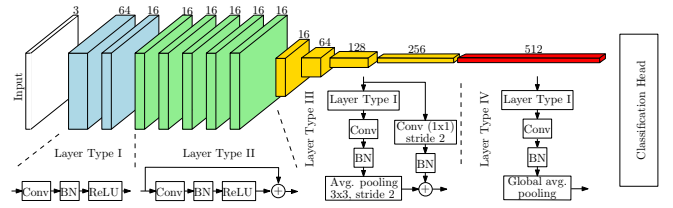


Figure 5: Overview of the SRNet, based on the illustration in [18].

The key part of the SRNet is the first seven layers, where no pooling operation is involved. Since pooling act as a low-pass filter, omitting it does not suppress the noise-like stego (age) signal. In [13], the SRNet was trained using different learning scenarios to investigate the influence of the presence of strong in-field sensor defects. The ‘five-crop-fusion’ learning scenario was the most position dependent scenario. This scenario was also utilized in [15] to analyze the influence of image content in deep learning based age approximation and is again used in this work.

In particular, five different SRNets are trained on patches ( $256 \times 256$ ) taken from a fixed position in the images. These positions are at the top left (‘tl’), the top right (‘tr’), the bottom left (‘bl’), the bottom right (‘br’) corners and in the center of the image (‘ce’). The final class prediction is obtained by fusing together the different outputs of the individual sub-models.

As already shown in [15], when a ‘standard’ SRNet is trained on regular scene images, inference is most likely based on image content. As a potential countermeasure, the following two different techniques are applied to mitigate the influence of image content **during training**.

#### 3.1 Median Filter Residuals

One way to reduce the interference of the image content is to preprocess the input data. For this purpose, one possibility is to apply a denoising filter  $F$ , and then obtained the residuals by subtracting the filtered image

from the original image, *i.e.*,  $R = Y - F(Y)$ . By considering a pixel’s dynamic range from 0 to 255, a single residual value  $R_i$  can have a value  $R_i \in \mathbb{Z} : -255 \leq R_i \leq 255$ . For this work, a median filter with kernel 3 is used as denoising filter  $F$ . To force the residuals to be in the same range as the pixel values, the absolute values are considered (*i.e.*,  $R = |Y - F(Y)|$ ).

### 3.2 Content Suppression Layer

The constrained convolutional layer [20] was introduced by Bayar et al. in the context of image manipulation detection. Usually, residuals are used in image manipulation detection techniques. For this reason, the authors propose to place a dedicated layer (*i.e.*, the constrained convolutional layer) at the beginning of a CNN. To enforce this layer to learn residuals, the following constraints

$$\begin{cases} w_k(0, 0) = -1 \\ \sum_{m,n \neq 0} w_k(m, n) = 1 \end{cases} \quad (8)$$

are applied to each of the  $K$  filters in the constraint convolution layer, where  $k$  denotes the  $k^{th}$  filter and the central weight  $w$  is denoted by spatial index (0,0). Since an RGB input is considered in this work and the magnitude of the age signal may vary between color channels, the described constraint is applied to each layer of the filter kernel.

## 4 Experiments

As described in section 3, the SRNet is trained in three different variants: (i) trained on regular images (SRNet-basic), (ii) trained on median filter residuals (SRNet-res) and, (iii) SRNet with a content suppression layer trained on regular images (SRNet-cs). First, these three variants are trained based on the generated synthetic images (with an age signal embedded). The results obtained by applying the proposed XAI technique are used to verify the functionality and act as a baseline. Second, the influence of image content is evaluated when the three described variants are trained on regular scene images. If preprocessing is applied (*i.e.*, SRNet-res), it is always applied (*i.e.*, to the training, validation and test set, as well as before creating the average images).

### 4.1 Dataset

The Northumbria Temporal Image Forensics (NTIF) [21] database is a publicly available dataset for temporal im-

age forensics. The NTIF dataset comprises images from 10 different cameras: two Canon IXUS115HS (Nc01 & Nc02), two Fujifilm S2950 (Nf01 & Nf02), two Nikon Coolpix L330 (Nn01 & Nn02), two Panasonic DMC TZ20 (Np01 & Np02) and two Samsung pl120 (Ns01 & Ns02). For each device, approximately 71 time-slots ranging over 94 weeks (between 2014 and 2016) are available. Further details about the dataset can be found in [21]. Images from this database are also used in other image forensics related publications, *i.e.*, [22, 23].

In the context of image age approximation, the NTIF database is used in [12, 14, 15, 24]. The authors in [12] divided the first 25 time-slots into five age classes. As already mentioned in the introduction (section 1), an overall classification accuracy of over 85% is reported for these five classes (by AlexNet with transfer learning mode). In this work, the same class definitions as in [12] are used. However, we consider only the first and last classes (*i.e.*, time-slot 1-5 and 21-25, respectively). Overall, there is a time difference of about 4 months between the two classes.

In addition, images from two of our own imagers, a Canon PowerShotA720IS (Pc01) and a Nikon E7600 (Pn01), are used. For both imagers, two classes are considered, with a time difference of about 12 and 15 years, respectively. Images from these two devices are also used in [14, 15, 9, 25, 13]. The two sets of DFIs used to generate the synthetic images were also acquired with these two imagers. However, these two sets were not taken at the same time as the regular scene images. There is about a 4 year time difference between the two DFI sets.

### 4.2 Experimental Settings

All different models are trained in the ‘five-crop-fusion’ approach (as described in section 3) over a fixed number of 180 epochs with a batch size of 4. The initial learning rate of 0.001 is decreased after 100 epochs to 0.0001. The ‘adamax’ [26] is used as an optimizer. During training, the class with fewer samples is oversampled accordingly.

A stratified sampling strategy is used, where 80% of the images per class are selected as train set. The remaining 20% are divided equally between a validation set and a test set. The evaluation is performed 8 times for each imager, with samples selected randomly and independently. We remind that the main contribution of this work is not to improve the classification results, but to highlight the problem of content bias.

To evaluate a trained model based on the proposed XAI approach, 20 different sets of average images are

generated per class, with 80% of all samples (including training, validation and testing data) randomly selected for each set. However, 80% of the samples are used only for the class with fewer samples. The other class is undersampled accordingly. This is to ensure that a balanced set is used to generate the average images.

### 4.3 Evaluation Metric

As described in section 2.1, the age signal in average images should be preserved while content is suppressed. For this reason, the separation performance of the trained model (when inference is based on an age signal) for average images should be similar to that for original inputs (*i.e.*, the images used to train the model, like regular scene images or median filter residuals). Similarity can be measured by the difference between two quantities. Hence, we compute the mean difference of accuracy values ( $\bar{\Delta}$ ) resulting from providing average images ( $acc^{\bar{Y}}$ ) and original inputs ( $acc^Y$ ), *i.e.*,

$$\bar{\Delta}(\bar{Y}) = \frac{1}{N} \sum_{i=1}^N (acc_i^Y - 0.5) - |acc_i^{\bar{Y}} - 0.5|, \quad (9)$$

where  $N$  denotes the number of runs. In the context of average images, the accuracy  $acc^{\bar{Y}}$  is considered as a measure of separability, where  $acc^{\bar{Y}} = 0$  and  $acc^{\bar{Y}} = 1$  indicates a perfect separation of the average images. Since the average images are balanced, an accuracy of 0.5 represents in terms of separability the worst case (in a binary classification problem, as considered in this work). For this reason an accuracy value of, for example, 0.2 and 0.8 can be considered equivalent in terms of separability. In equation (9) this is expressed by the term  $|acc_i^{\bar{Y}} - 0.5|$ . An accuracy of less than 0.5 may occur when providing average images because the pixel value distribution of the average images differs from the distribution of the images (regular images or median filter residuals) used for training. The term  $(acc_i^Y - 0.5)$  is used to bring the accuracy obtained by the original inputs into the same range.

If the model has learned to exploit an age signal,  $\bar{\Delta}(\bar{Y})$  and  $\bar{\Delta}(\bar{Y}_r)$  should be approximately zero. In contrast,  $\bar{\Delta}(\bar{Y}_c) \approx 0$  would indicate that most likely content is exploited, since  $\bar{Y}_c$  is strongly dependent on image content. If age traces in high-frequency image components (*e.g.*, in-field sensor defects) are exploited,  $\bar{\Delta}(\bar{Y}_f)$  should be clearly greater than zero. In addition, an  $\bar{\Delta}(\bar{Y}) < 0$  indicates that the accuracy based on the average images is better than based on the original input. However, since

neural network can be considered a ‘black box’, there is no exact threshold for  $\bar{\Delta}(\cdot)$  that rules out exploited content bias.

### 4.4 Experimental Results

Before analyzing the results obtained when applying the proposed XAI method, Fig. 6 illustrates the classification accuracy obtained (on the test set) when the models are trained on synthetic images. With the SRNet-basic variant, better classification than random prediction is only possible with 3/8 runs for the Pn01. This already indicates that it is difficult for a ‘standard’ CNN trained on raw pixel values to exploit the subtle age traces, even if distractions from the image content can be ruled out. With the variants SRNet-res and SRNet-cs, perfect discrimination is possible for almost all runs.

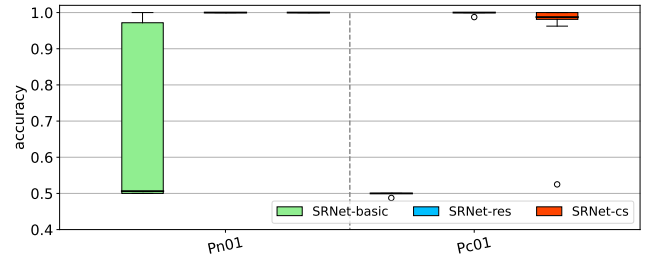


Figure 6: Classification accuracy, when the models are trained on synthetic images.

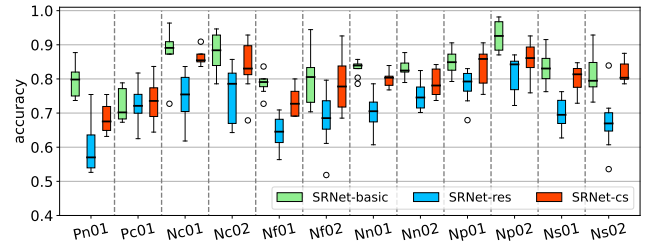


Figure 7: Classification accuracy, when the models are trained on regular images.

Table 1 shows the results obtain when applying the proposed XAI method. As expected, if separation is possible based on original input (*i.e.*,  $acc^Y > 0.5$ ), separation based on average images ( $\bar{Y}$ ) and the structural components of the average images ( $\bar{Y}_r$ ) is equally possible (*i.e.*,  $\bar{\Delta}(\cdot) \approx 0$ ). However, if median filter residuals are used for training (SRNet-res),  $\bar{Y}_r$  seems to yield the



Table 1: Mean difference of accuracy values ( $\overline{\Delta}$ ), when the models are trained on synthetic images. The last row represents the average value of the individual columns.

IDs	SRNet-basic					SRNet-res					SRNet-cs				
	$\overline{\Delta}(\overline{Y})$	$\overline{\Delta}(\overline{Y}_c)$	$\overline{\Delta}(\overline{Y}_r)$	$\overline{\Delta}(\overline{Y}_f)$	$\overline{acc}^Y$	$\overline{\Delta}(\overline{Y})$	$\overline{\Delta}(\overline{Y}_c)$	$\overline{\Delta}(\overline{Y}_r)$	$\overline{\Delta}(\overline{Y}_f)$	$\overline{acc}^Y$	$\overline{\Delta}(\overline{Y})$	$\overline{\Delta}(\overline{Y}_c)$	$\overline{\Delta}(\overline{Y}_r)$	$\overline{\Delta}(\overline{Y}_f)$	$\overline{acc}^Y$
Pn01	-0.02	0.18	-0.00	0.18	0.68	0.00	0.50	0.00	0.50	1.00	0.00	0.50	0.00	0.50	1.00
Pc01	<b>0.00</b>	<b>0.00</b>	<b>0.00</b>	<b>0.00</b>	<b>0.50</b>	<b>0.06</b>	0.50	<b>-0.00</b>	0.50	1.00	-0.00	0.43	-0.00	0.42	0.93
	-0.01	0.09	-0.00	0.09	0.59	0.03	0.50	-0.00	0.50	1.00	-0.00	0.47	-0.00	0.46	0.97

Table 2: Mean difference of accuracy values ( $\overline{\Delta}$ ), when the models are trained on regular images. The last row represents the average value of the individual columns.

IDs	SRNet-basic					SRNet-res					SRNet-cs				
	$\overline{\Delta}(\overline{Y})$	$\overline{\Delta}(\overline{Y}_c)$	$\overline{\Delta}(\overline{Y}_r)$	$\overline{\Delta}(\overline{Y}_f)$	$\overline{acc}^Y$	$\overline{\Delta}(\overline{Y})$	$\overline{\Delta}(\overline{Y}_c)$	$\overline{\Delta}(\overline{Y}_r)$	$\overline{\Delta}(\overline{Y}_f)$	$\overline{acc}^Y$	$\overline{\Delta}(\overline{Y})$	$\overline{\Delta}(\overline{Y}_c)$	$\overline{\Delta}(\overline{Y}_r)$	$\overline{\Delta}(\overline{Y}_f)$	$\overline{acc}^Y$
Pn01	0.16	0.16	0.33	0.16	0.83	0.37	0.24	0.32	0.27	0.91	0.25	0.43	0.29	0.43	0.93
Pc01	0.18	0.15	0.25	0.18	0.75	0.41	0.41	0.29	0.41	0.91	0.14	0.43	0.13	0.38	0.93
Nc01	0.26	0.39	0.27	0.38	0.96	0.33	0.23	0.20	0.19	0.92	0.19	0.47	0.19	0.44	0.97
Nc02	0.47	0.41	0.47	0.47	0.97	0.33	0.29	0.21	0.28	0.95	0.26	0.47	0.27	0.47	0.97
Nf01	0.10	0.28	0.35	0.19	0.85	0.40	0.40	0.21	0.34	0.91	0.27	0.45	0.35	0.45	0.95
Nf02	0.27	0.31	0.26	0.29	0.82	0.40	0.41	0.21	0.29	0.91	0.11	0.45	0.20	0.40	0.95
Nn01	0.30	0.39	0.39	0.39	0.89	0.43	0.43	0.32	0.33	0.93	0.37	0.46	0.45	0.46	0.96
Nn02	<b>-0.01</b>	<b>0.06</b>	0.36	0.02	0.86	0.45	0.32	0.14	0.01	0.95	0.37	0.46	0.43	0.46	0.96
Np01	0.44	0.44	0.21	0.44	0.94	0.35	0.15	0.06	0.24	0.95	<b>0.06</b>	<b>0.46</b>	<b>0.07</b>	<b>0.43</b>	<b>0.96</b>
Np02	0.48	0.48	0.10	0.48	0.98	0.29	0.24	0.28	0.32	0.96	0.20	0.47	0.11	0.37	0.97
Ns01	0.25	0.28	0.38	0.25	0.88	0.43	0.39	0.13	0.35	0.93	<b>0.04</b>	<b>0.46</b>	<b>0.24</b>	<b>0.43</b>	<b>0.96</b>
Ns02	0.34	0.34	0.31	0.34	0.84	0.37	0.42	0.33	0.23	0.93	0.38	0.46	0.41	0.46	0.96
	0.27	0.31	0.31	0.30	0.88	<b>0.38</b>	<b>0.33</b>	<b>0.23</b>	0.27	0.93	0.22	0.45	0.26	0.43	0.95

more stable results (blue values). A separation based on average color ( $\overline{Y}_c$ ) and the filtered average image ( $\overline{Y}_f$ ) is not possible (*i.e.*,  $\overline{acc}^Y - \overline{\Delta}(\cdot) \approx 0.5$ ). This is reasonable since most likely in-field sensor defects are exploited by the network. The constant difference  $\overline{\Delta} = 0$  (red values) is due to the fact that the classification of the original inputs was not possible for all runs (*i.e.*,  $\overline{acc}^Y = 0.5$ ). Based on the results, it can be stated that the method works as expected.

The obtained accuracy values (on the test set) when using regular scene images for training are shown in Figure 7. In contrast to the results based on synthetic images, the best accuracy is reached when no content mitigation is applied (SRNet-basic). This is reasonable if inference is based mainly on the image content. The results in Table 2 also support this suggestion. In principle,  $\overline{\Delta}(\overline{Y})$  is relatively high for all imagers except Nn02 (red values). With this device, the accuracy is even a bit better based on average images ( $\overline{Y}$ ). However, the accuracy based on the average color ( $\overline{Y}_c$ ) is similarly high. Since there is basically no age signal present in the av-

erage color, similar accuracy with the average color indicates that image content is exploited in this case as well.

Looking at the average values across all devices (last row), the image content seems to play a significant role in all variants evaluated. Nevertheless, the SRNet-cs variant performs ‘best’ in the comparison. Furthermore, is noticeable that separation in the SRNet-res variant (blue values) works better with average color ( $\overline{Y}_c$ ) than with average images ( $\overline{Y}$ ). This is surprising, since the color is strongly suppressed in median filter residuals. As observed with the baseline results,  $\overline{Y}_r$  seems to yield the more stable results with the SRNet-res variant (magenta value).

Compared to the variants and imagers evaluated, the SRNet-cs variant when trained on images of Np01 and Ns01 (green values) seems most likely to learn an age signal (*i.e.*, a low value of  $\overline{\Delta}(\overline{Y})$  combined with a high value of  $\overline{\Delta}(\overline{Y}_c)$ ). In both cases also high-frequency parts of the average image are relevant (*i.e.*, high values of  $\overline{\Delta}(\overline{Y}_f)$ ). This could indicate that probably in-field sen-

sensor defects are exploited. In contrast to Np01, the value shift caused by the generation of  $\bar{Y}_r$  affects the separation performance of the SRNet-cs trained on Ns01 images.

## 5 Conclusion

Content bias is an open problem in the context of deep learning age approximation. Based on the experiment conducted, we have seen that it is difficult for a ‘standard’ SRNet to exploit the subtle age traces, even if it is not distracted by a content bias in the training data. In this work, we proposed a method that evaluates the influence of image content (based on average images). The functionality of this method was validated using models trained on synthetic images (where content bias can be ruled out). Based on this approach, we showed that a ‘standard’ SRNet trained on regular images is strongly dependent on image content. Even if content mitigation techniques are applied (*i.e.*, SRNet-res and SRNet-cs), the image content still plays an important role. Only in the SRNet-cs variant, when the model is trained on images from 2/12 imagers, it seems that an age signal could be exploited.

## References

- [1] G. H. Chapman, R. Thomas, Z. Koren, I. Koren, Empirical formula for rates of hot pixel defects based on pixel size, sensor area, and ISO, in: R. Widenhorn, A. Dupret (Eds.), *Sensors, Cameras, and Systems for Industrial and Scientific Applications XIV*, Vol. 8659, Int. Society for Optics and Photonics, SPIE, 2013, pp. 119 – 129. doi:10.1117/12.2005850.
- [2] G. H. Chapman, R. Thomas, R. Thomas, K. J. Coelho, S. Meneses, T. Q. Yang, I. Koren, Z. Koren, Increases in hot pixel development rates for small digital pixel sizes, *Electronic Imaging 2016* (12) (2016) 1–6.
- [3] J. Leung, G. H. Chapman, I. Koren, Z. Koren, Characterization of gain enhanced in-field defects in digital imagers, in: *2009 24th IEEE Int. Symposium on Defect and Fault Tolerance in VLSI Systems*, 2009, pp. 155–163.
- [4] J. Leung, G. H. Chapman, Z. Koren, I. Koren, Statistical identification and analysis of defect development in digital imagers, in: B. G. Rodricks, S. E. Süsstrunk (Eds.), *Digital Photography V*, Vol. 7250, Int. Society for Optics and Photonics, SPIE, 2009, pp. 272 – 283. doi:10.1117/12.806109.
- [5] J. Leung, J. Dudas, G. H. Chapman, I. Koren, Z. Koren, Quantitative analysis of in-field defects in image sensor arrays, in: *22nd IEEE Int. Symposium on Defect and Fault-Tolerance in VLSI Systems (DFT 2007)*, IEEE, 2007. doi:10.1109/dft.2007.59.
- [6] A. J. Theuwissen, Influence of terrestrial cosmic rays on the reliability of ccd image sensors part 1: Experiments at room temperature, *IEEE Transactions on Electron Devices* 54 (12) (2007) 3260–3266.
- [7] A. J. Theuwissen, Influence of terrestrial cosmic rays on the reliability of ccd image sensors part 2: Experiments at elevated temperature, *IEEE Transactions on Electron Devices* 55 (9) (2008) 2324–2328.
- [8] J. Fridrich, M. Goljan, Determining approximate age of digital images using sensor defects, in: N. D. Memon, J. Dittmann, A. M. Alattar, E. J. Delp, III (Eds.), *Media Watermarking, Security, and Forensics III*, Vol. 7880, Int. Society for Optics and Photonics, SPIE, 2011, pp. 49 – 59. doi:10.1117/12.872198.
- [9] R. Joechl, A. Uhl, A machine learning approach to approximate the age of a digital image, in: *Digital Forensics and Watermarking: 19th Int. Workshop, IWDW 2020, Melbourne, VIC, Australia, November 25–27, 2020, Revised Selected Papers*, Vol. 12617 of Springer LNCS, Springer Int. Publishing, 2021, pp. 181–195.
- [10] A. Krizhevsky, I. Sutskever, G. E. Hinton, Imagenet classification with deep convolutional neural networks, *Advances in neural information processing systems* 25 (2012) 1097–1105.
- [11] C. Szegedy, W. Liu, Y. Jia, P. Sermanet, S. Reed, D. Anguelov, D. Erhan, V. Vanhoucke, A. Rabinovich, Going deeper with convolutions, in: *Proceedings of the IEEE Conf. on computer vision and pattern recognition*, 2015, pp. 1–9.
- [12] F. Ahmed, F. Khelifi, A. Lawgaly, A. Bouridane, Temporal image forensic analysis for picture dating with deep learning, in: *2020 Int. Conf. on*



Computing, Electronics Communications Engineering (iCCECE), 2020, pp. 109–114. doi:10.1109/iCCECE49321.2020.9231160.

- [13] R. Joechl, A. Uhl, Apart from in-field sensor defects, are there additional age traces hidden in a digital image?, in: 2021 IEEE Int. Workshop on Information Forensics and Security (WIFS), Montpellier, France, 2021, pp. 1–6.
- [14] R. Joechl, A. Uhl, Device (in)dependence of deep learning-based image age approximation, in: 2022 ICPR-Workshop on Artificial Intelligence for Multimedia Forensics and Disinformation Detection, Montreal, Quebec, Canada, 2022, pp. 1–14.
- [15] R. Jöchel, A. Uhl, Deep learning image age approximation-what is more relevant: Image content or age information?, in: Digital Forensics and Watermarking: 21st Int. Workshop, IWDW 2022, Guilin, China, November 18-19, 2022, Revised Selected Papers, Springer, 2023, p. 114–128.
- [16] P. Linardatos, V. Papastefanopoulos, S. Kotsiantis, Explainable ai: A review of machine learning interpretability methods, *Entropy* 23 (1) (2021) 18.
- [17] S. R. Richter, V. Vineet, S. Roth, V. Koltun, Playing for data: Ground truth from computer games, in: Computer Vision–ECCV 2016: 14th European Conf., Amsterdam, The Netherlands, October 11-14, 2016, Proceedings, Part II 14, Springer, 2016, p. 102–118.
- [18] M. Boroumand, M. Chen, J. Fridrich, Deep residual network for steganalysis of digital images, *IEEE Transactions on Information Forensics and Security* 14 (5) (2018) 1181–1193.
- [19] K. He, X. Zhang, S. Ren, J. Sun, Deep residual learning for image recognition, in: Proceedings of the IEEE Conf. on computer vision and pattern recognition, 2016, pp. 770–778.
- [20] B. Bayar, M. C. Stamm, Constrained convolutional neural networks: A new approach towards general purpose image manipulation detection, *IEEE Transactions on Information Forensics and Security* 13 (11) (2018) 2691–2706.
- [21] F. Ahmed, F. Khelifi, A. Lawgaly, A. Bouridane, The ‘northumbria temporal image forensics’ database: Description and analysis, in: 2020 7th Int. Conf. on Control, Decision and Information Technologies (CoDIT), Vol. 1, 2020, pp. 982–987. doi:10.1109/CoDIT49905.2020.9263888.
- [22] M. Al-Ani, F. Khelifi, On the spn estimation in image forensics: A systematic empirical evaluation, *IEEE Transactions on Information Forensics and Security* 12 (5) (2017) 1067–1081.
- [23] A. Lawgaly, F. Khelifi, Sensor pattern noise estimation based on improved locally adaptive dct filtering and weighted averaging for source camera identification and verification, *IEEE Transactions on Information Forensics and Security* 12 (2) (2017) 392–404. doi:10.1109/TIFS.2016.2620280.
- [24] F. N. Ahmed, F. Khelifi, A. Lawgaly, A. Bouridane, A machine learning-based approach for picture acquisition timeslot prediction using defective pixels, *Forensic Science Int.: Digital Investigation* 39 (2021) 301311.
- [25] R. Joechl, A. Uhl, Identification of in-field sensor defects in the context of image age approximation, in: 2021 IEEE Int. Conf. on Image Processing (ICIP), Anchorage, AK, USA, 2021, pp. 3043–3047. doi:10.1109/ICIP42928.2021.9506023.
- [26] D. P. Kingma, J. Ba, Adam: A method for stochastic optimization (2017). arXiv:1412.6980.